Stabilization of hexagonal close-packed metallic nickel for alumina-supported systems prepared from Ni(II) glycinate

Vicente Rodríguez-González[a], Eric Marceau[a,*], Patricia Beaunier[a], Michel Che[a,c], Cyrille Train[b]

[a]*Laboratoire de Réactivité de Surface (UMR 7609 CNRS), Université Pierre et Marie Curie-Paris 6, 4 Place Jussieu, 75252 Paris Cedex 05, France*
[b]*Laboratoire de Chimie Inorganique et Matériaux Moléculaires (UMR 7071 CNRS), Université Pierre et Marie Curie-Paris 6, 4 Place Jussieu, 75252 Paris Cedex 05, France*
[c]*Institut Universitaire de France, France*

Abstract

The decomposition in flowing argon of the neutral complex $[Ni^{II}(glycinate)_2(H_2O)_2]$ leads to a mixture of face-centered cubic (fcc) and hexagonal close-packed (hcp) metallic nickel. The latter is the main phase when the Ni(II) complex is supported on alumina. Unlike most hexagonal Ni phases described earlier, and similar to hexagonal Ni_3C, the unit cell parameters ($a = 0.2493$ and $c = 0.4084$ nm) lead to Ni–Ni distances equal to those encountered in fcc Ni. TEM shows that the nanoparticles are protected by graphite layers, whose elimination by heating in hydrogen results in transformation to the fcc phase and crystal growth. Magnetic measurements provide evidence of the coexistence of superparamagnetic and ferromagnetic nanoparticles. This result is in line with the broad size distribution observed by TEM and is interpreted on the basis of the metallic character of hcp Ni particles.
© 2006 Elsevier Inc. All rights reserved.

Keywords: Nickel; Alumina; Glycinate; Hexagonal close-packed arrangement; X-ray diffraction; Transmission electron microscopy; Electron diffraction; Magnetic measurements

1. Introduction

The preparation of oxide-supported metal catalysts generally involves the deposition of a precursor metal salt from an aqueous solution which wets a porous support [1]. For reasons of cost, availability and solubility, nitrates of hexaaqua complexes are mostly used as precursor salts for metals ranging from manganese to zinc. Upon thermal treatment in air, supported crystals of precursors salts are transformed into oxide particles, which, in the case of nickel or cobalt, can be reduced by hydrogen into metal nanoparticles able to catalyse hydrogenation reactions [2,3].

Alternative methods of depositing metal particles on a support include (i) deposition-precipitation, where metal particles are obtained by reduction of supported hydroxide- or silicate-like species formed by slow basification of the precursor solution [4,5]; and (ii) use of precursor salts where metal ions are initially bonded to organic chelating ligands in order to favour their dispersion upon deposition [6,7]. In the latter method, chosen for this work, it is possible to use an inert atmosphere to promote the direct self-reduction of the precursor compound to the metallic state, with hydrogen released by the chelating ligands during thermal treatment [8].

The formation of supported nanoparticles leads to contrasting results for nickel or cobalt. While Ni nanoparticles appear as face-centered cubic (fcc), like for bulk metal, cobalt nanoparticles exhibit both fcc and/or hexagonal close-packed (hcp) arrangements depending on catalyst history and particle size. Bulk cobalt crystallizes in the hcp phase while the fcc phase is only metastable in ambient conditions [9–11].

This paper shows that polymorphism also exists for nickel, provided that the Ni nanoparticles are prepared by

*Corresponding author. Fax: +33 1 44 27 60 33.
E-mail address: eric.marceau@upmc.fr (E. Marceau).

decomposition of nickel(II) glycinate in an inert atmosphere. Moreover, the hexagonal phase becomes dominent when nickel(II) glycinate has been initially supported on alumina. The hcp structure is evidenced by diffraction methods and by comparison of the lattice parameters and magnetic properties with data previously published on related systems.

2. Experimental

2.1. Catalyst preparation

The neutral metal complex $[Ni^{II}(glycinate)_2(H_2O)_2]$, in short $Ni(gly)_2$ with $gly = NH_2CH_2COO^-$, was prepared following a procedure adapted from the literature [12]. One gram of $Ni(OH)_2$ prepared by precipitation of $NiCl_2 \cdot 6H_2O \cdot$ (Aldrich, 99.99%) with KOH (Prolabo) was introduced under stirring into 100 mL of a solution containing 1.62 g of glycine NH_2CH_2COOH (Aldrich, 99.99%) at 80 °C (molar ratio glycine/Ni = 2). Within 1 min, the solution turned blue upon reaction between $Ni(OH)_2$ and glycine. After 15 min, the warm solution was filtered in order to eliminate traces of unreacted nickel hydroxide ($<5\%$). The filtrate was concentrated to fifty milliliters and cooled down to room temperature. 50 mL of ethanol (Prolabo) were added under stirring. Within a few minutes, blue crystals of $Ni(gly)_2$ precipitated. The solution was left under stirring for 30 min and allowed to stand overnight, after which crystals were collected by filtration and dried in a static oven at 60 °C. [Yield: 55%. Found: Ni, 23.84; C, 19.63; N, 11.40; H, 4.99 wt%. Calc. for $[Ni(C_2H_4NO_2)_2(H_2O)_2]$: Ni, 24.19; C, 19.78; N, 11.54; H, 4.94 wt%].

Two catalysts (named Ni15 and Ni28 after their Ni weight content determined after thermal treatment in argon) were prepared by impregnation of γ-alumina (EC 1285 of Institut Français du Pétrole; $\varnothing = 150–250 \mu m$, specific surface area $= 200 \, m^2 \, g^{-1}$, void volume determined by water impregnation $= 0.68 \, cm^3 \, g^{-1}$). One gram of alumina was introduced into 15 and 30 mL, respectively, of a $0.2 \, mol \, L^{-1}$ solution of $Ni(gly)_2$, prepared by dissolution of the complexes at 60 °C and left to cool to room temperature before contact with the support. After 1 h under stirring, water was eliminated by slow evaporation at 80 °C under reduced pressure (ca 0.1 bar), in order to obtain a homogeneous distribution of $Ni(gly)_2$ crystals on alumina and to avoid separate crystallization. Moist solids were dried in static air at 80 °C over 12 h. Diffractograms of dried samples were checked for peaks characteristic of $Ni(gly)_2$, the three most intense being located at $2\theta = 13.04$, 16.94 and 18.80°. Dried samples were then thermally treated in argon flow ($100 \, mL \, min^{-1}$) up to 500 °C ($7.5 °C \, min^{-1}$), and kept 1 h at that temperature. Other thermal treatments are detailed in the Results section.

2.2. Catalyst characterization

Elemental analyses were performed (CNRS Service of Analysis, Vernaison, France) by ICP for Ni, and by catharometry for C and N after fast calcination of the sample in air. Powder X-ray diffraction (XRD) measurements were performed with a Siemens D500 diffractometer, using Cu Kα radiation (1.5418 Å). Diffraction data were analysed by the Rietveld method, using the fully automated code RIETQUAN [13]. X-ray diffraction was also used to assess Ni crystalline domains sizes ($\varnothing > 3 \, nm$) after thermal treatment, by applying the Laue-Scherrer equation to peaks corresponding to a single Bragg diffraction. Transmission electron micrographs (TEM) and selected area electron diffraction (SAED) were collected with a JEOL 100 CXII UHR microscope. Magnetic measurements were performed at 10 and 300 K with a Quantum Design MPMS-5S SQUID magnetometer in the DC mode at external magnetic field up to 5 T.

3. Results

Elemental compositions after drying and thermal treatment in argon are gathered in Table 1. After drying, the stoichiometry (i.e., C/Ni and N/Ni atomic ratios) of the supported complexes is close to that of $Ni(gly)_2$. After thermal treatment in argon, the main feature is the presence of carbon due to incomplete ligand decomposition (compare with the value relative to the unsupported complex). The argon flow rate used for thermal treatment being identical for both samples, less carbon is eliminated from Ni28, which initially contained twice the organic molecules of Ni15.

Fig. 1 shows X-ray diffractograms (a–c) of alumina and the supported systems after thermal treatment in argon; and difference diffractograms (d, e) obtained after subtracting the alumina contribution. Difference diffractograms can be compared with those (f, g) of two reference compounds: unsupported $Ni(gly)_2$ after thermal decomposition in argon and fcc metallic Ni, respectively.

Table 1
Elemental composition of unsupported and supported systems after drying and thermal treatment in argon

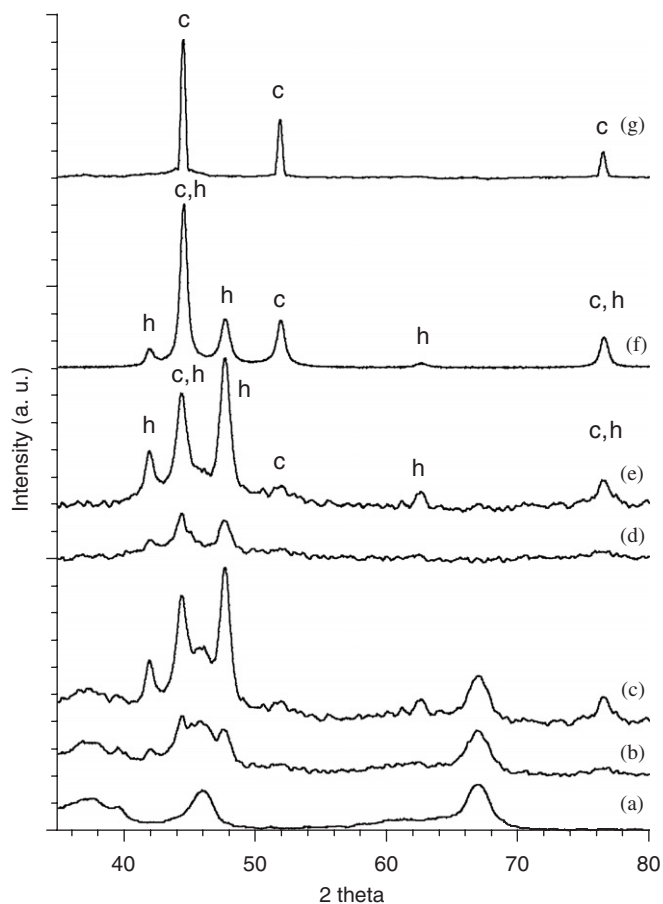| Sample	Ni (wt%)	C (wt%)	C/Ni atomic ratio	N (wt%)	N/Ni atomic ratio
After drying					
Complex alone	23.84	19.63	4.0	11.40	2.0
Ni15	10.90	7.90	3.6	4.53	1.7
Ni28	15.60	12.17	3.8	6.66	1.8
After thermal treatment in argon					
Complex alone	79.00	18.50	1.1	1.19	<0.1
Ni15	15.35	0.30	0.1	0.13	<0.1
Ni28	27.50	5.06	0.9	0.97	0.1

Fig. 1. X-ray diffractograms of : (a) alumina; (b) Ni15 after thermal treatment in flowing Ar; (c) Ni28 after thermal treatment in flowing Ar; (d) difference between Ni15 and alumina; (e) difference between Ni28 and alumina; (f) unsupported [Ni(gly)$_2$(H$_2$O)$_2$] after thermal treatment in flowing Ar; (g) reference fcc Ni. Diffractograms (b) and (c) have been normalized with respect to alumina. "c" refers to the face-centered cubic Ni phase and "h" to the hexagonal Ni phase.

Some XRD peaks of diffractograms (d–f) can be assigned to fcc Ni ($2\theta = 44.35$, 51.91 and 76.42°), while others ($2\theta = 41.83$, 47.66 and 62.56°) come from another phase. In particular, the most intense peak of Ni28 is observed at $2\theta = 47.66°$, in contrast to what is expected for fcc Ni ($2\theta = 44.57°$). By analogy with lines positions for hexagonal Ni$_3$C and Co (JCPDS 6-0697 and 5-0727, respectively), the positions of five out of the six diffraction lines observed could be fitted to an hexagonal unit cell (i.e., lines visible on Fig. 1e and f except the line at $2\theta = 51.91°$). The following relationship linking Miller indices (hkl), a, c and interplanar spacings d(hkl) of the hexagonal system was used [14]:

$$d(hkl) = a / \left[4/3(h^2 + hk + k^2) + (l \times a/c)^2 \right]^{1/2}.$$

A good fit with experimental values was obtained for $a = 0.2493$ and $c = 0.4084$ nm; the indexed peaks are presented in Table 2.

In order to check the validity of the parameters and reproduce the relative intensities of the peaks, Rietveld fits

Table 2
Assignment of diffraction lines on the basis of an hexagonal system with $a = 0.2493$ and $c = 0.4084$ nm

2θ (°)	d_{exp} (nm)	d_{calc} (nm)	Reflection
41.830	0.2159	0.2159	(010)
44.350	0.2042	0.2042	(200)
47.660	0.1908	0.1909	(011)
62.560	0.1485	0.1484	(012)
76.420	0.1246	0.1246	(110)

were performed on diffractograms e and f of Fig. 1, by combining two components: a Ni hexagonal phase (space group $P6_3/mmc$) characterized by the parameters given above, and the stable Ni fcc phase (space group $Fm\bar{3}m$) with $a = 0.3524$ nm consistent with literature data [15]. Diffractogram d (sample Ni15) was not taken into account as far as refinements were concerned, because of poorly resolved peaks.

As displayed on Fig. 2a, a very satisfactory fit is reached for the unsupported compound, based on $70 \pm 1\%$ of fcc Ni and $30 \pm 1\%$ of hexagonal Ni (R_{wp}: 0.15, R_b: 0.15, R_{exp}: 3.4%). On the basis of Rietveld and Laue-Scherrer analyses of lines at $2\theta = 47.66$ and 51.91°, the average sizes of the crystalline domains were found to be 10 and 13 nm for hexagonal and fcc Ni, respectively.

The accuracy of the fit is lower for Ni28 (R_{wp}: 0.83, R_b: 0.83, R_{exp}: 4.0%) (Fig. 2b), because of uncertainties due to the higher signal-to-noise ratio, to differences in width of the peaks of hexagonal and fcc Ni, and to subtraction of the alumina contribution. However, it appears that the major supported phase detected by XRD is hexagonal Ni ($70 \pm 10\%$), while fcc Ni is the minor phase ($30 \pm 10\%$). A separate experiment shows that when crystals of Ni(gly)$_2$ are mechanically mixed with dried Ni28, the proportion of fcc Ni after thermal treatment increases (the line at $2\theta = 44.5°$ becomes prominent). The stabilization of hexagonal Ni is thus related to the initial dispersion of the complexes on alumina upon impregnation.

The average crystalline domains size on Ni28 is evaluated to be about 10 nm for hexagonal Ni. The average size is difficult to calculate for the fcc phase, due to the poorly resolved line at $2\theta = 51.91°$. This line is nevertheless broader than those of hexagonal Ni, implying the presence of smaller particles, with a distribution centered between 4 and 7 nm, according to Rietveld and Laue-Scherrer analyses, respectively.

TEM micrographs give a more complete view of the composition of Ni28. Most pictures show Ni particles with different shapes and sizes (5–40 nm) and alumina platelets embedded in a matrix (Fig. 3a) which disappears upon a 1 h post-treatment in pure hydrogen at 500 °C, with the same conditions of gas flow and temperature ramp used for argon treatment (Fig. 3b). At higher magnification, the graphitic nature of this matrix whose interlayer spacing is measured to be 0.33 nm (JCPDS 41-1487) is confirmed (Fig. 3c and d).
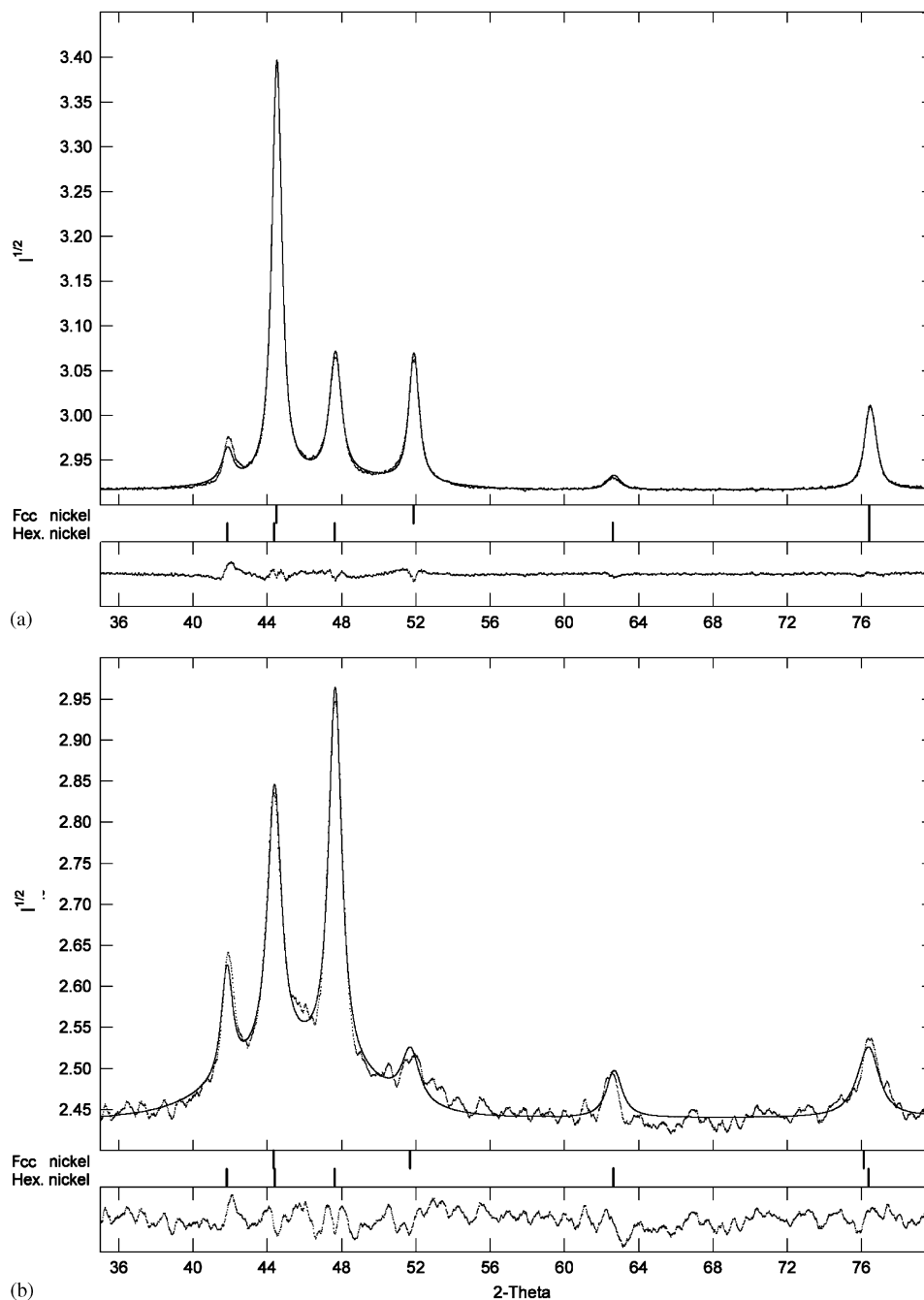
Fig. 2. Rietveld fits for: (a) unsupported system after thermal treatment in flowing Ar; (b) sample Ni28 after thermal treatment in flowing Ar.

The crystalline nature of a typical assembly of 5–30 nm Ni particles (Fig. 4a) was established by electron diffraction (Fig. 4b). Three main diffraction rings are visible (Fig. 4c), in line with the group of three close diffraction lines characteristic of hexagonal Ni (see Fig. 2). Reciprocical distances r_1, r_2 and r_3 are in the ratio 1:1.04:1.10, close to the ratios found for the associated interspacing distances $d_3 = 0.1908$, $d_2 = 0.2042$ and $d_1 = 0.2159$ nm (1:1.07:1.13). Absolute d-spacings calculated from the electron diffraction pattern after calibration based on diffraction by gold (scale presented in Fig. 4b) are in good agreement with XRD results: $d_1 = 0.194$, $d_2 = 0.201$ and $d_3 = 0.214$ nm.

The Ni28 diffractogram is unchanged if the 1 h plateau in flowing Ar at 500 °C is skipped. Furthermore, the diffractogram is not modified after storing the sample at room temperature in ambient atmosphere for 1 year. Hexagonal Ni is also detected for Ni28, though to a lesser extent, when the thermal treatment after drying is carried out in pure hydrogen instead of argon (Fig. 5b).

In contrast, only fcc Ni is present on Ni15 exposed to these conditions (Fig. 5a), as is the case for both catalysts when the above-mentioned H_2 post-treatment at 500 °C follows the thermal treatment in argon (Fig. 5c and d). The effect of treatment in hydrogen is two-fold: elimination of
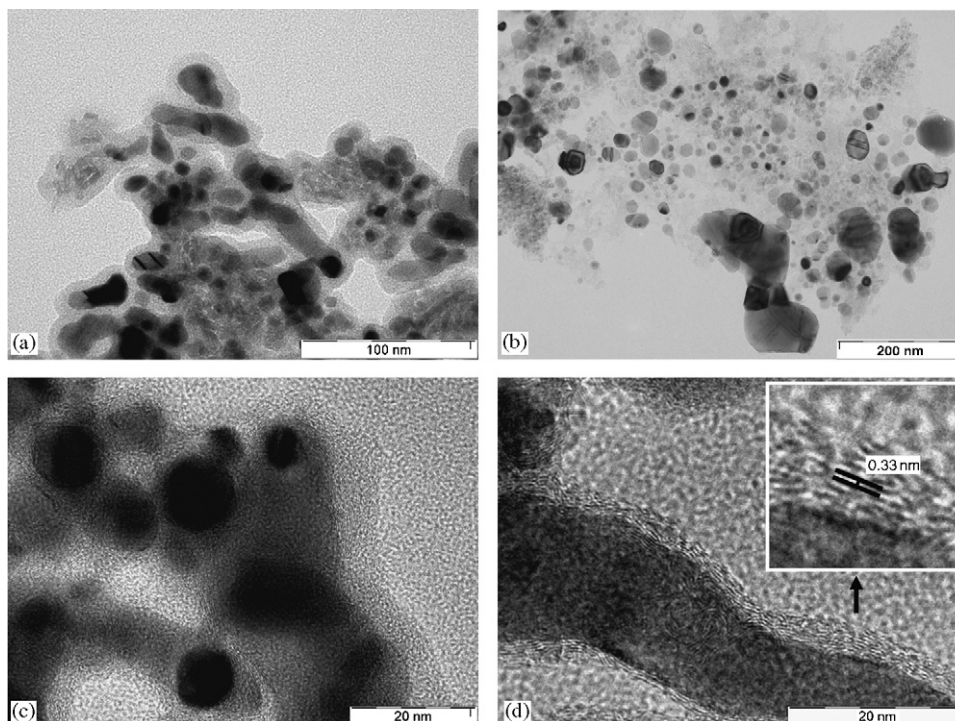
Fig. 3. TEM micrographs : (a) general view of sample Ni28 after treatment in Ar; (b) general view of sample Ni28 after 1 h post-treatment in H_2; (c) detail exhibiting the graphite layers embedding Ni particles; (d) close-ups on graphite layers.
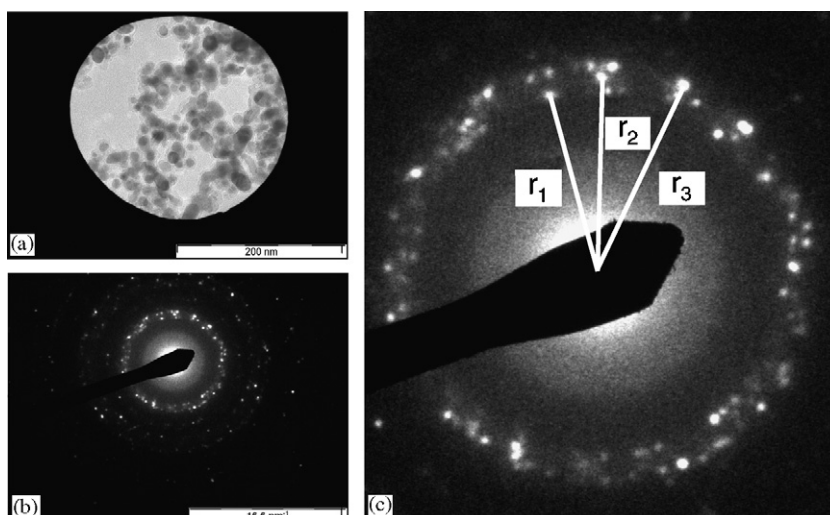

Fig. 4. (a) TEM micrograph of sample Ni28 after treatment in Ar, (b) selected-area electron diffraction pattern of the region presented in (a), (c) detail of the electron diffraction pattern.

carbon from the samples, with atomic ratio C/Ni below 0.2 on Ni28, and sintering of Ni particles, as evidenced by narrower diffraction lines and larger crystals (TEM) of 8–50 nm with the major fraction above 20 nm (Fig. 3b).

Fig. 6 shows magnetization (M) vs. field (H) plots measured for Ni28 at 300 and 10 K, and expressed in emu/g_{Ni}. Saturation magnetizations (M_s) at 300 and 10 K, respectively, represent 50% and 70% of the values obtained for bulk metallic Ni (close to 55 emu/g_{Ni}) [16–18]. At both temperatures, a hysteresis loop is observed

which is narrower at 300 K ($H_c = 40$ Oe) than at 10 K (382 Oe). It was confirmed that the shape of the curve at 300 K could not be modelled using Langevin functions [16], showing that the results cannot be interpreted on the basis of superparamagnetism alone, suggesting a ferromagnetic behaviour.

However, at 10 K saturation is not observed at the highest maximum field (5 T). The increase of the curve slope is characteristic of a superparamagnetic population—at lower temperatures, thermal energy opposes less to the
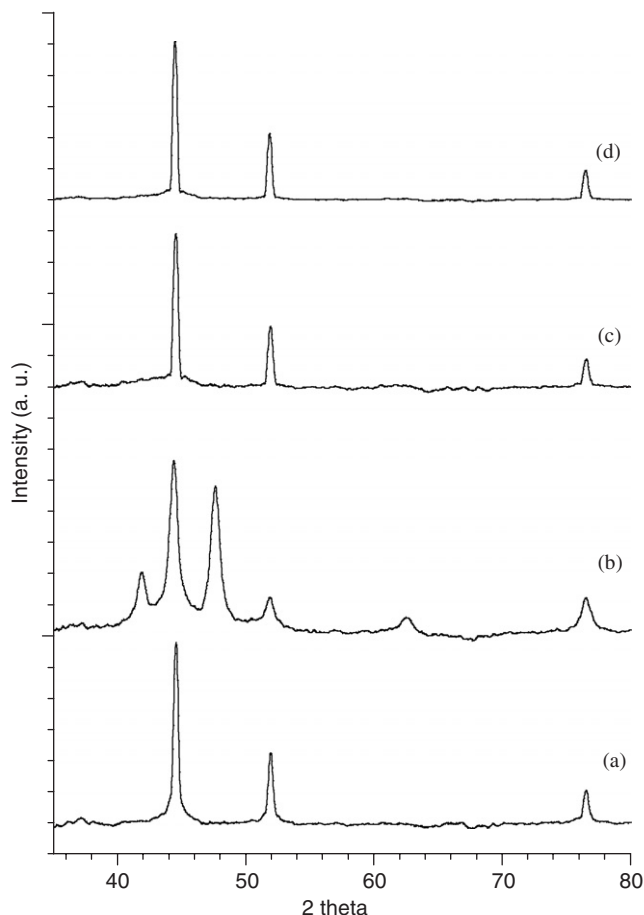
Fig. 5. X-ray difference diffractograms of: (a) Ni15 after direct thermal treatment in H_2; (b) Ni28 after direct thermal treatment in H_2; (c) Ni15 after thermal treatments in Ar and then H_2; (d) Ni28 after thermal treatments in Ar and then H_2.

action of magnetic field—indicating coexistence of several magnetic behaviours. Some nanoparticles are ferromagnetic up to 300 K, while others are superparamagnetic with blocking temperatures < 300 K.

4. Discussion

4.1. Identification of nickel hcp phase

While Ni particles mostly crystallize in the fcc structure, the less common hexagonal phase has been reported, the common feature being the nanometer scale at which metal particles or films have been prepared (Table 3). As a matter of fact, Ni_3C and Ni_3N crystallize in the hexagonal systems and some studies mention that the possible contamination of the metal by impurities may have promoted the fcc to hcp transformation [14,19,21].

Most of the unit cell parameters of Table 3 are indeed close to those of Ni_3C. The fact that the c/a ratio approaches the value of $(8/3)^{1/2} = 1.63$, characteristic of close-packed arrangement, has been used as an argument in favour of a purely metallic character of the phase obtained [15]. However, assuming a hcp phase, a parameter
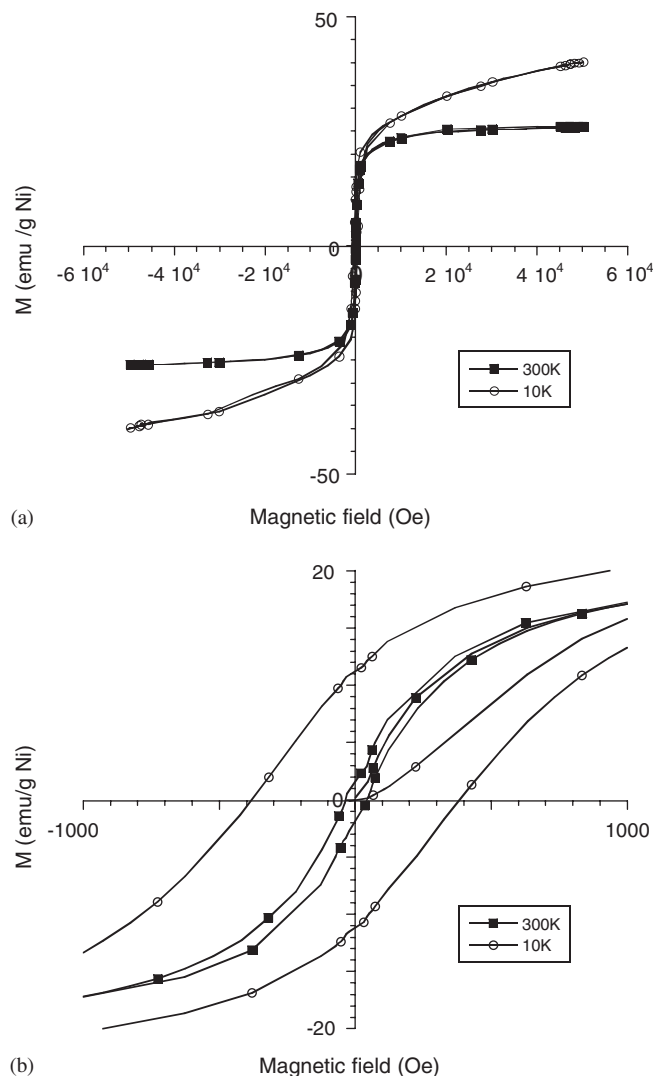

Fig. 6. (a) Magnetization vs. field plots for Ni28 at $T = 10$ and 300 K; (b) zoom on the lower fields region.

a_{hex} larger than 0.26 nm would lead to a Ni covalent radius $r(Ni) = a_{hex}/2$ larger than 0.13 nm. This is inconsistent with the value calculated from close-packed fcc arrangement characterized by $a_{cub} = 0.3524$ nm: $r(Ni) = a_{cub}\sqrt{2}/4 = 0.1246$ nm. By contrast, 0.1246 nm is the value obtained when $r(Ni)$ is calculated from the hexagonal structure described in our work; closest Ni–Ni distances (0.2493 nm) are accordingly equivalent in both fcc and hcp arrangements.

In agreement with only two earlier studies [23, 24], the present work suggests that the hcp Ni phase is not necessarily stabilized by the presence of atoms inserted in the bulk. It however differs on two points with these previous works (Table 3): (i) the larger organized crystalline domains, 10 nm compared to a maximum of 4 nm [24] and (ii) the absence of the metallic substrate (hcp Co) used to stabilize the hcp phase [23]. The hypothesis of cobalt impurities inducing the formation of hcp Ni can be discarded, because alloyed Ni–Co nanoparticules retain

Table 3
Literature data for hexagonal Ni structural characteristics

Ref.	Synthesis	a (nm)	c (nm)	c/a	Particles size (nm)
15	$Ni(acac)_2$ + K-B alloy	0.2653	0.4348	1.64	20
19	Nickel chloride + KBH_4 in ethylenediamine (autoclave)	0.2653	0.4348	1.64	Not mentioned, agglomerates > 200 nm (TEM)
20	Thermal decomposition of Ni_3C_{1-x} phases	0.2650	0.4400	1.66	< 15
14	Evaporation of Ni	0.2622	0.4320	1.65	20
21	Evaporation of Ni	0.2620	0.4310	1.64	500
22	Evaporation of Ni	0.2440	0.4220	1.73	< 3 nm
23	Electrodeposition of Ni	0.2500	0.3975	1.59	100
24	Ni(II) salt + NaH + t-BuOH	0.2440	0.3960	1.62	⩽4
This work	*Thermal decomposition of Ni(II) glycinate*	*0.2493*	*0.4084*	*1.64*	*10*

Ref.	Reference compounds	a (nm)	c (nm)	c/a	
14	Ni_3N	0.2667	0.4312	1.62	
21	Ni_3C	0.2628	0.4306	1.64	

the fcc structure at least up to 60 wt% cobalt [25–27]. The (001) face of MgO as substrate has also been reported to stabilize hcp Ni clusters, but the large c/a ratio indicates that the structure is not close-packed due to the adjustment of the lattice constants to match those of the oxidic support [22].

4.2. Origin and stabilization of the hcp phase

The hcp phase originates from the decomposition of $Ni(gly)_2$, as the experiment with the unsupported complex suggests, where it is the minor phase. The initial dispersion of $Ni(gly)_2$ crystals on alumina leads a stabilization of a higher proportion of hcp Ni. However, the presence of alumina is not sufficient to explain this stabilization, which disappears upon hydrogen post-treatment. As far as quantification is concerned, it must be noted that XRD and TEM are silent for particles with $\varnothing < 3$ nm, whose formation can be favoured by support-enhanced dispersion compared with the unsupported compound. In agreement with Illy et al. [24], we may assume that hcp phase is also present for smaller particles and that the relative proportions of hcp and fcc Ni determined by Rietveld analysis are realistic with regard to the whole of Ni^0 formed.

The protection of Ni particles by graphite seems to be the key factor for both the stabilization of the hcp phase and its thermal stability up to 500 °C. The polymorphic transformation from hcp to fcc Ni and concomitant sintering in hydrogen are indeed eased when the initial quantity of carbon on the catalyst is low (compare Ni15 and Ni28, Fig. 5a and b, respectively). The thermal stability is another difference with the systems described previously [15,21,28], where the hcp to fcc transformation occurs at 420–450 °C, as in the case of Ni_3C [29]. In the present work, carbon stabilizes hcp particles by external templating rather than by insertion, as observed earlier for the stabilization of hcp Pd [30] and Pt [31] and assumed for

particles derived from Ni_3C [20]. These structure-directing and protective roles of carbon are amplified on alumina, because residues released during decomposition of organic ligands can be retained by the high-surface area oxide support and surround Ni species dispersed during impregnation.

The stabilization could be also explained by a "surfactant effect" [24]: adsorbed molecules may modify the surface energy of metallic clusters during growth, eventually favouring the hcp phase. This hypothesis may not apply to $Ni(gly)_2$ decomposition, because organic solvents and reactants (THF, mesitylene, t-BuONa) used in earlier work [24] chemically differ from glycine. This mode of formation of hcp nanoparticles, below 100 °C, is valid not only for Ni(II) carboxylate, but also for Ni(II) chloride. The reduction of Ni(II) by a NaH/t-BuOH mixture has also been used for alumina-supported precursor salts [32], resulting in hcp Ni particles active in catalytic hydrogenation without pretreatment, suggesting they were not covered with carbon, a major difference with our system. However, it is not known if their structure was modified upon exposure to hydrogen.

4.3. The role of the glycinate ligand

One may question why glycinate favours the formation of hcp Ni, in contrast to other hydrogen- and carbon-containing chelating ligands, such as ethylenediamine (en), which favour the fcc phase [8]. When en is used, the decomposition of the supported salts includes elimination of en ligands but also of Ni(II) counterions, e.g. nitrates, which collectively contribute to disruption of the crystals.

Neutral $Ni(gly)_2$ decomposes in two steps, first by elimination of water at 120 °C (above which crystals retain their coherence by coordinating oxygens from free C=O bonds to neighbouring Ni(II) ions), then by decomposition of glycinate at 330 °C [33,34]. Unlike salts containing en,

there are no nitrate counterions in the neutral $Ni(gly)_2$ complex to promote ligands decomposition into gaseous compounds such as CO, NO and H_2O as reported earlier [8,35]. We may assume that upon thermal treatment in inert atmosphere, residues from glycinate trapped on alumina polymerize around Ni nanoparticles, leading to the carbon layers which protect the hcp phase. Systems in which carbon coats or encapsulates Ni particles have also been prepared by Ni evaporation [16,17] or reduction of NiO at 600 °C [36], but in these cases the formation of the more stable fcc phase was promoted.

4.4. Magnetic properties

Table 4 allows one to compare the magnetic properties of sample Ni28 to those of bulk Ni ($\varnothing \geqslant 3000$ nm) and nanoparticles. Most of these systems involve fcc Ni, in interaction with carbon or not. In the only report on hcp Ni [19], the similarity with the values obtained for Ni_3C [29] suggests that the former was contaminated by carbon, in line with our critical survey of XRD data.

The remanence ratio (M_s) and H_c measured for Ni28 are consistent with those reported earlier for 10–15 nm carbon-covered or carbon-free Ni particles [16,37]. The lower value of M_s for nanoparticles than for bulk Ni has been explained by three related arguments: (i) a size effect at the nanometric scale, i.e., a relatively larger number of surface atoms leading to a weaker magnetic moment than the core (for instance see in Table 4 the M_s decrease with

size for samples described in Zhang et al. [18]); (ii) a lack of crystallinity for small particles [40]; (iii) the existence of a non-magnetic "dead layer" [18], assigned to the aforementioned non-crystalline fraction or to the presence of a poorly magnetic "nickel carbide"-like layer [29].

The thickness of the magnetically inactive layer t has been linked to the diameter $\varnothing$ and saturation magnetization M_s via: $M_s = M_s(\text{Ni bulk}) (1-6t/\varnothing)$ [18], leading in our case to a relative thickness of the layer of 5–8% of $\varnothing$, i.e., < 1 nm for a 10 nm Ni particle. This result confirms that for Ni28, magnetic measurements can be interpreted on the basis that the largest fraction of Ni, hcp and fcc, is present as metal and is magnetically active, though possibly surrounded by a minor carbide fraction, not detected by XRD.

The change of magnetic behaviours between 10 and 300 K can be linked to the broad distribution of Ni particles, in terms of size and relative localization. The largest particles as well as agglomerates of particles engaged in dipolar magnetic interactions can appear as ferromagnetic at room temperature [41]. Because the blocking temperature decreases with size, some smaller particles, superparamagnetic at 300 K, become ferromagnetic for measurement made at 10 K. Their coercive force, as well as their remanent magnetization, increase for decreasing temperature, explaining the observed global increase of H_c and M_s. Finally, a high surface-to-volume ratio makes saturation of magnetisation of the smallest particles difficult even at 10 K.

Table 4
Literature data on the magnetic properties of Ni nanoparticles

T (K)	System	Size (nm)	M_s (emu/g_{Ni})	Remanence ratio	H_c (Oe)	Ref.
300	Ni (fcc)	75000	51.3	0.13	104	[17]
	Ni (fcc)	3000	55	0.05	100	[16]
	Ni (fcc) in C nanotubes covered with C	100	nd	0.25	384	[36]
	Ni (fcc) coated with C	30–40	49.6	0.32	199	[17]
	Ni (fcc) in C nanotubes	19	nd	0.31	525	[36]
	Ni (fcc) covered with O	10–15	43.7	0.38	265	[16]
	Ni (fcc) coated with C	10–15	22.5	0.06	7	[16]
	Ni (fcc)	12	32	0.16	40	[37]
	Ni (fcc)	9	22	0.29	0.1	[38]
	Ni (hcp)	nd	7.4	0.12	94	[19]
	Ni_3C (hcp)	10	0.8	0.12	70	[29]
	Ni28	*10*	*26*	*0.08*	*40*	*This work*
10	Ni (fcc) coated with C	10–15	25.2	0.29	316	[16]
	Ni (fcc) covered with O	10–15	46.8	0.44	500	[16]
	Ni_3C (hcp)	10	1.4	0.40	500	[29]
	Ni28	*10*	*40*	*0.28*	*382*	*This work*
5	Ni (fcc)	3000	57.6			[18]
	Ni (fcc)	59	53.3	0.37	280	[18]
	Ni (fcc)	46	47.8	0.34	340	[18]
	Ni (fcc)	22	28.7	0.37	352	[18]
	Ni (fcc)	4	27.7	0.05	200	[39]

nd: not determined.

5. Conclusions

The decomposition of [Ni^{II}(glycinate)$_2$(H$_2$O)$_2$] in flowing argon leads to dimorphic Ni metal particles: the usual stable fcc phase, and a hexagonal close-packed (hcp) phase, which becomes dominent when Ni(II) complexes are dispersed on alumina. In the latter case, X-ray diffraction, TEM and magnetic measurements suggest that the hcp core is surrounded by a "nickel carbide"-like layer and protected by graphite layers. The stability of hcp particles is attributed to the templating effect from carbon located outside the particles and originating from the decomposition of glycinate ligands. These results confirm both the existence of hcp Ni nanoparticles up to a size of 20 nm and the stabilization of this phase by carbon. Unlike most systems described earlier, this stabilization does not involve inserted carbon atoms.

References

[1] (a) M. Che, C.O. Bennett, Adv. Catal. 36 (1989) 55;
    (b) J.F. Lambert, M. Che, J. Mol. Catal. A 162 (2000) 5.
[2] H. Pines, Adv. Catal. 35 (1987) 323.
[3] H. Schulz, Top. Catal. 26 (2003) 73.
[4] P. Burattin, M. Che, C. Louis, J. Phys. Chem. B 101 (1997) 7060.
[5] P. Burattin, M. Che, C. Louis, J. Phys. Chem. B 102 (1998) 2722.
[6] J.Y. Carriat, M. Che, M. Kermarec, M. Verdaguer, A. Michalowicz, J. Am. Chem. Soc. 120 (1998) 2059.
[7] A.J. van Dillen, R.J.A.M. Terörde, D.J. Lensveld, J.W. Geus, K.P. de Jong, J. Catal. 216 (2003) 257.
[8] F. Négrier, E. Marceau, M. Che, D. de Caro, C.R. Chimie, 6 (2003) 231.
[9] D. Bazin, L. Guczi, J. Lynch, Appl. Catal. A 226 (2002) 87.
[10] N.O. Elbashir, P. Dutta, A. Manivannan, M.S. Seehra, C.B. Roberts, Appl. Catal. A 285 (2005) 169.
[11] G.L. Bezemer, P.B. Radstake, V. Koot, A.J. Van Dillen, J.W. Geus, K.P. de Jong, J. Catal. 237 (2006) 291.
[12] D.N. Sen, S. Mizushima, C. Curran, J.V. Quagliano, J. Am. Chem. Soc. 77 (1955) 211.
[13] L. Lutterotti, R. Ceccato, R. Dal Maschio, E. Pagani, Mater. Sci. Forum (1998) 278.
[14] P. Hemenger, H. Weik, Acta Crystallogr. 19 (1965) 690.
[15] G. Carturan, G. Cocco, S. Enzo, R. Ganzerla, M. Lenarda, Mater. Lett. 7 (1988) 47.
[16] X.C. Sun, X.L. Dong, Mater. Res. Bull. 37 (2002) 991.
[17] P.Z. Si, Z.D. Zhang, D.Y. Geng, C.Y. You, X.G. Zhao, W.S. Zhang, Carbon 41 (2003) 247.
[18] H.T. Zhang, G. Wu, X.H. Chen, X.G. Qiu, Mater. Res. Bull. 41 (2006) 495.
[19] Y. Mi, D. Yuan, Y. Liu, J. Zhang, Y. Xiao, Mater. Chem. Phys. 89 (2005) 359.
[20] V.I. Zaikovskii, V.V. Chesnokov, R.A. Buyanov, Kinet. Catal. 42 (2001) 813.
[21] C. Bonnelle, F. Vergand, Acta Crystallogr. 21 (1966) 1001.
[22] W. Tian, H.P. Sun, X.Q. Pan, J.H. Yu, M. Beadon, B.B. Boothroyd, Y.P. Feng, R.A. Lukaszew, R. Clarke, Appl. Phys. Lett. 86 (2005) 131915.
[23] J.G. Wright, J. Goddard, Philos. Mag. 11 (1965) 485.
[24] S. Illy, O. Tillement, F. Machizaud, J.M. Dubois, F. Massicot, Y. Fort, J. Ghanbaja, Philos. Mag. A 79 (1999) 1021.
[25] D. Golodnitsky, Y. Rosenberg, A. Ulus, Electrochim. Acta 47 (2002) 2707.
[26] G. Qiao, T. Jing, N. Wang, Y. Gao, X. Zhao, J. Zhou, W. Wang, Electrochim. Acta 51 (2005) 85.
[27] G. Mattei, C. de Julián Fernández, P. Mazzoldi, C. Sada, G. De, G. Battaglin, C. Sangregorio, D. Gatteschi, Chem. Mater. 14 (2002) 3440.
[28] D.L. Leslie-Pelecky, X.Q. Zhang, S.H. Kim, M. Bonder, R.D. Rieke, Chem. Mater. 10 (1998) 164.
[29] L. Yue, R. Sabiryanov, E.M. Kirkpatrick, D.L. Leslie-Pelecky, Phys. Rev. B 62 (2000) 8969.
[30] J. Walter, M. Nishioka, S. Hara, Chem. Mater. 13 (2001) 1828.
[31] J. Walter, J. Heiermann, G. Dyker, S. Hara, H. Shioyama, J. Catal. 189 (2000) 449.
[32] X. Jurvilliers, R. Schneider, Y. Fort, J. Ghanbaja, Appl. Organomet. Chem. 17 (2003) 161.
[33] G. D'Ascenzo, W.W. Wendlandt, Thermochim. Acta 13 (1975) 341.
[34] C.A. McAuliffe, W.D. Perry, J. Chem. Soc. A (1969) 634.
[35] F. Négrier, E. Marceau, M. Che, J.M. Giraudon, L. Gengembre, A. Löfberg, J. Phys. Chem. B 109 (2005) 2836.
[36] J. Cheng, X. Zhang, Y. Ye, J. Solid State Chem. 179 (2006) 91.
[37] D.H. Chen, C.H. Hsieh, J. Mater. Sci. 12 (2002) 2412.
[38] S.H. Wu, D.H. Chen, J. Colloid Interf. Sci. 259 (2003) 282.
[39] Y. Hou, S. Gao, J. Mater. Sci. 13 (2003) 1510.
[40] M.J. Bonder, E.M. Kirkpatrick, T. Martin, S.J. Kim, R.D. Rieke, D.L. Leslie-Pelecky, J. Magn. Magn. Mater. 222 (2000) 70.
[41] T. Ould Ely, C. Amiens, B. Chaudret, E. Snoeck, M. Verelst, M. Respaud, J.M. Broto, Chem. Mater. 11 (1999) 526.